nature geoscience

Supplementary information

A giant and persistent source of abiotic H_2 and CH_4 driven by slab rehydration

In the format provided by the
authors and unedited

This file includes:

Supplementary Figures

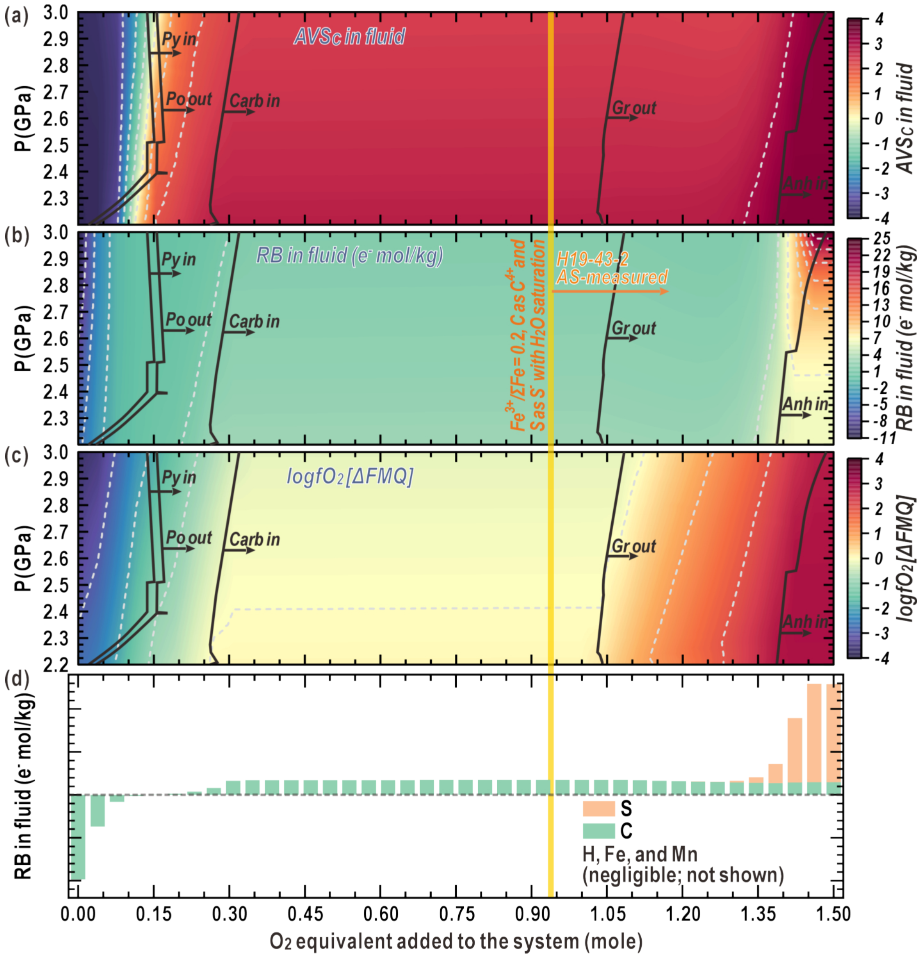

Supplementary Fig. 1. Evolution of the average valence state of carbon (AVS$_C$) in fluid, $\overline{RB}$ (mol/kg) in fluid, and fO_2 under fluid–saturated conditions, as functions of pressure and progressive addition of O_2 equivalents to the system.

(a) AVS$_C$ in fluid. (b) $\overline{RB}$ in fluid. (c) fO_2. (d) Distribution of the $\overline{RB}$ among fluid species at 2.8 GPa. Light gray dashed lines denote contours of AVS$_C$, $\overline{RB}$, and fO_2. The starting composition for the modeling is based on the RB reference of the eclogite (H19-43-2). Mineral stability fields involving pyrite (Py), pyrrhotite (Po), carbonate (Carb), garnet (Gr), and anhydrite (Anh) are indicated.

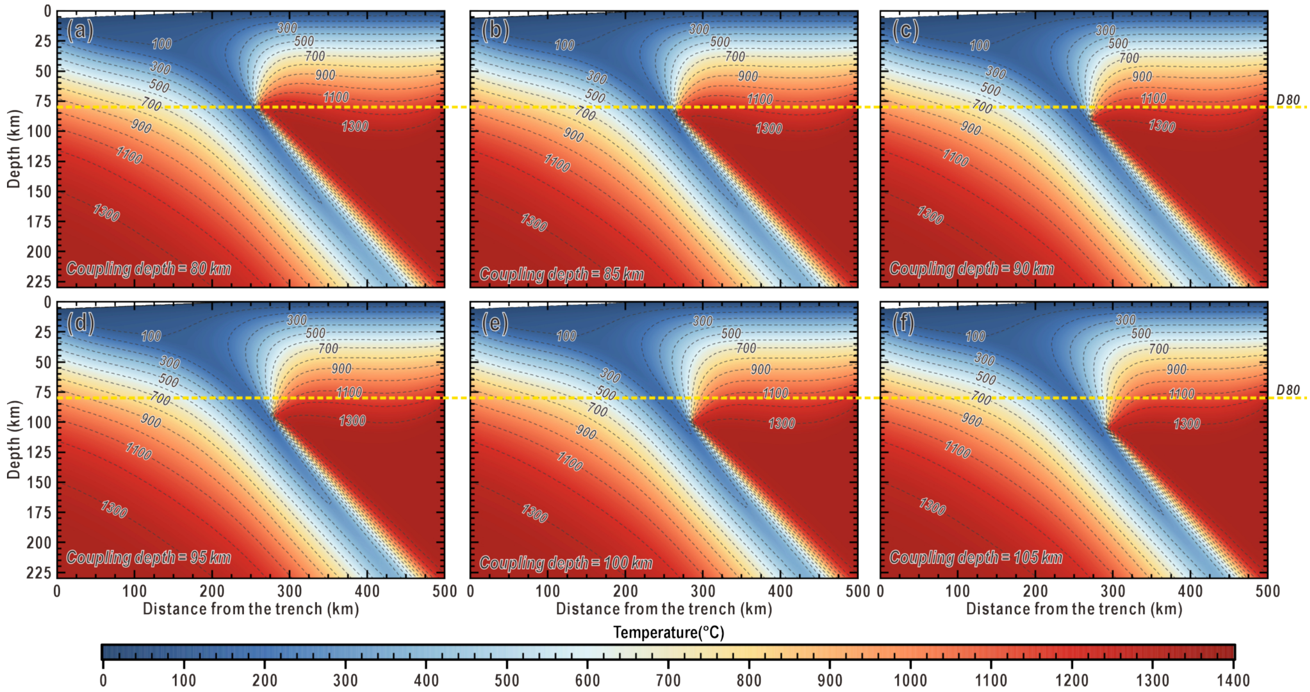

Supplementary Fig. 2. Modeled subduction-zone thermal structures for different depths of the decoupling–to–coupling transition, calculated using the finite–element framework from the FEniCS–SZ repository.

(a) 80 km. (b) 85 km. (c) 90 km. (D) 95 km. (E) 100 km. (F) 105 km.

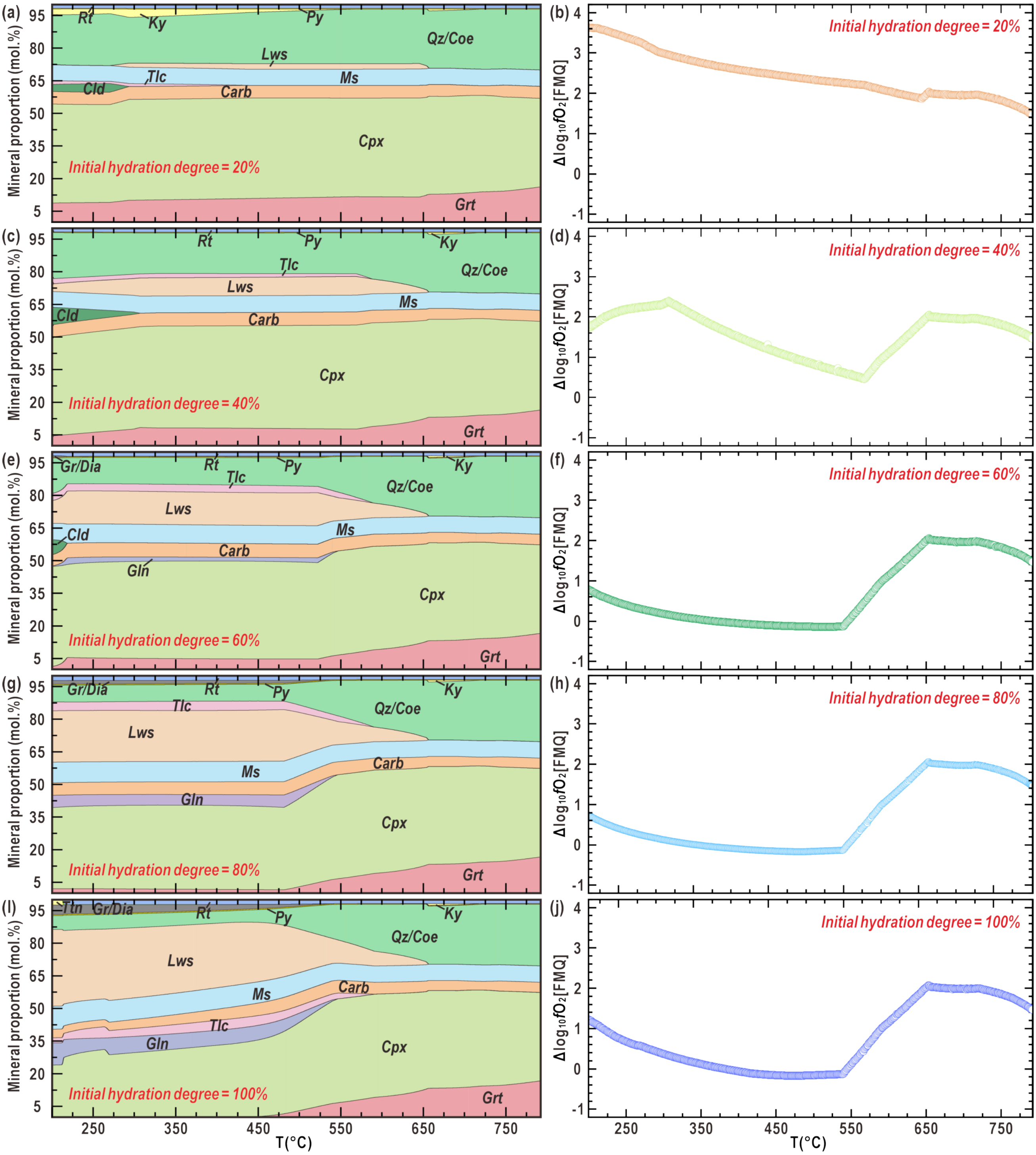

Supplementary Fig. 3. Mineral assemblage and oxygen fugacity (*f*O_2) variations during devolatilization for different initial rock hydration degrees.

(a) and (b) 20%. (d) and (d) 40%. (e) and (f) 60%. (g) and (h) 80%. (i) and (j) 100%. Thermodynamic modeling was performed using the measured bulk composition of CH_4–H_2-bearing eclogite along slab–top P–T paths in the southwestern Tianshan oceanic subduction zone. Oxygen fugacity is reported as $\log_{10}(fO_2)$ relative to the fayalite–magnetite–quartz (FMQ) buffer. Mineral abbreviations: Coe–coesite, Lws–lawsonite, Ms–muscovite, Carb–carbonate, Tlc–talc, Gln–glaucophane, Cpx–clinopyroxene, Grt–garnet, Ttn–titanite, Gr–graphite, Dia–diamond, Rt–rutile, Py–pyrite, Ky–kyanite, Qz–quartz.

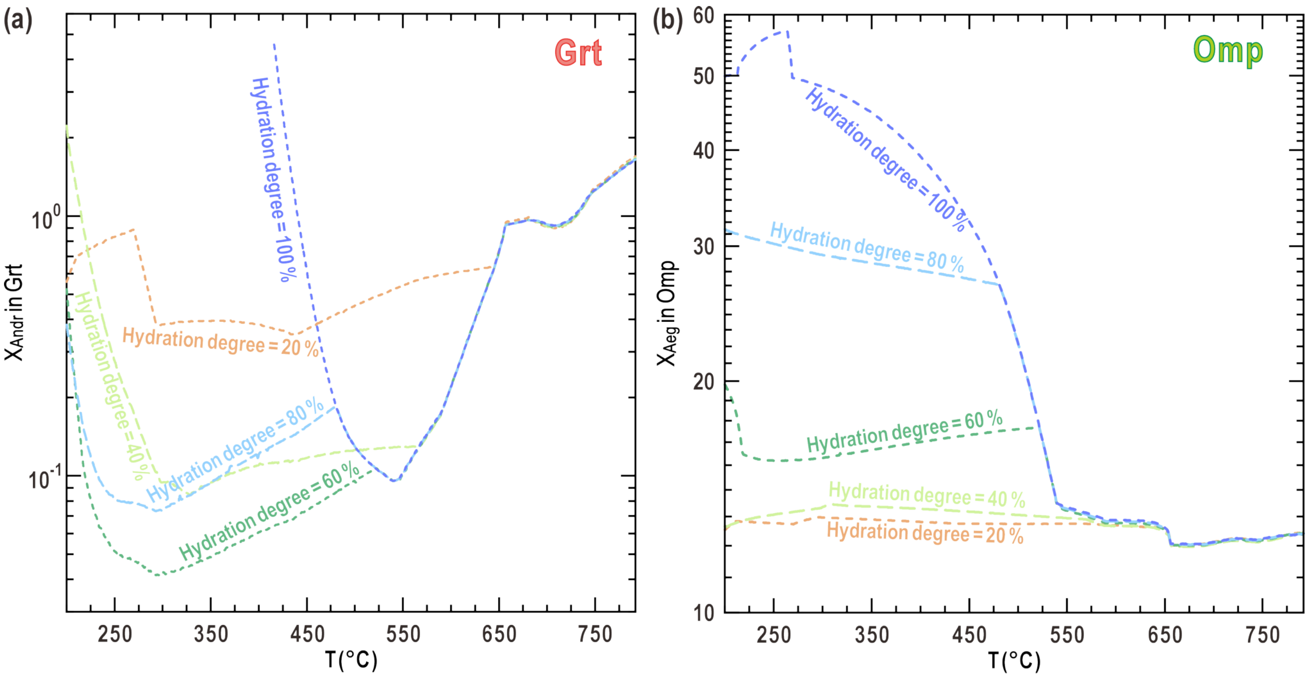

Supplementary Fig. 4. Modeled variations in mineral compositions with temperature along the slab–top P–T path for different initial hydration states of the rock.

(a) X_{Andr} in garnet. (b) X_{Aeg} in omphacite. Here, $X_{Andr} = \frac{100 \times Ca \times Fe^{3+}}{2 \times (Fe^{2+} + Fe^{3+} + Ca + Mg + Mn)}$; X_{Aeg} is calculated for the M1 site as $\frac{100 \times Fe^{3+}}{Fe^{2+} + Fe^{3+} + Al + Mg}$. Mineral abbreviations: Grt–garnet, Omp–omphacite, Andr–andradite; Aeg–aegirine.

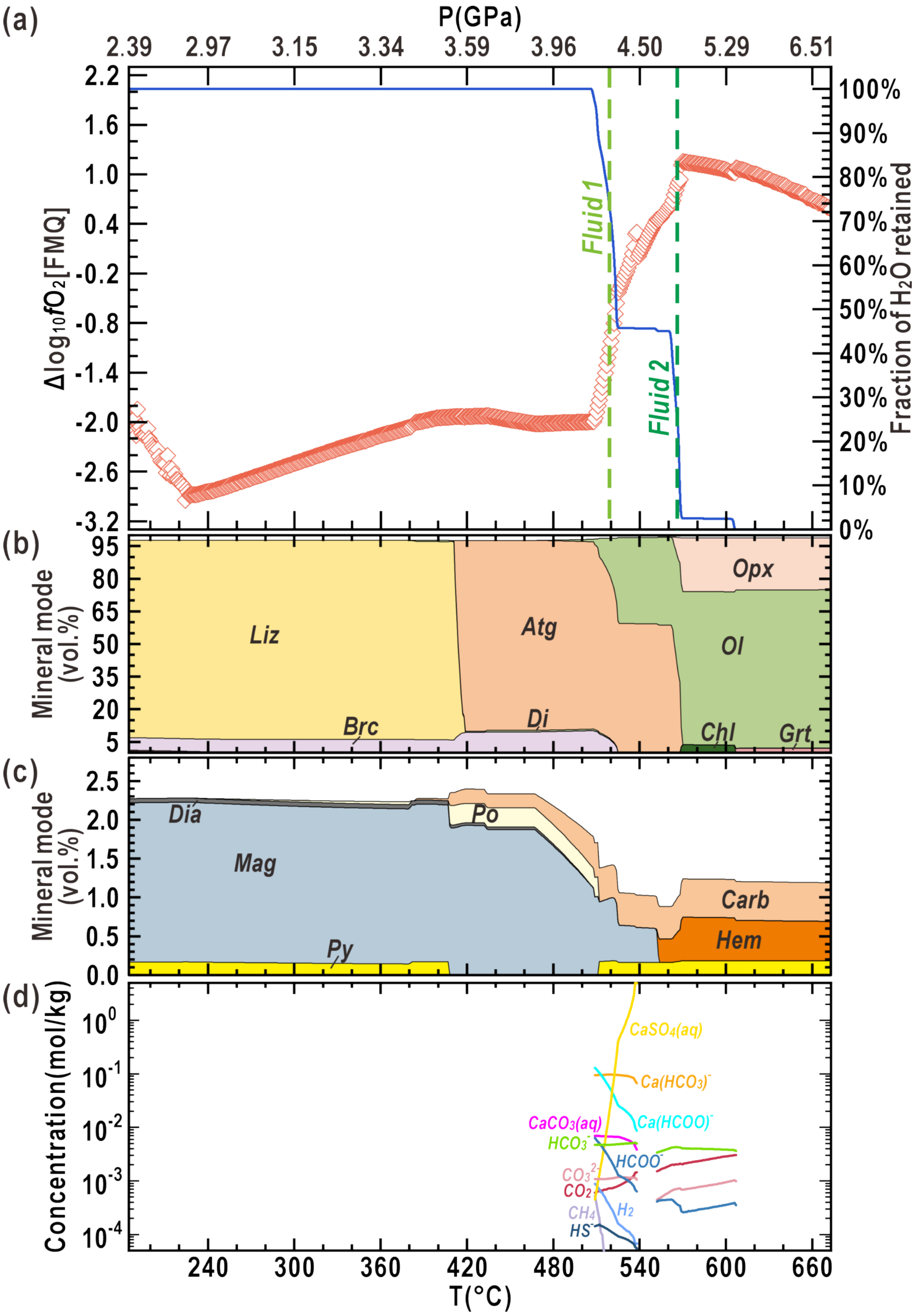

Supplementary Fig. 5. Modeled variations in oxygen fugacity, mineral assemblages, and fluid compositions along the slab–Moho P–T path during serpentinite devolatilization.

(a) Oxygen fugacity. (b) Silicate minerals. (c) C– and S-bearing phases and iron oxides. Mineral abbreviations: Liz–lizardite, Brc–brucite, Atg–antigorite, Di–diopside, Opx–orthopyroxene, Ol–olivine, Chl–chlorite, Grt–garnet, Dia–diamond, Mag–magnetite, Py–pyrite, Po–pyrrhotite, Carb–carbonates, Hem–hematite.

Supplementary Tables

Supplementary Table 1. Fluid speciation and corresponding average valence states of variable–valence elements used in this study.

Fluid speciation in DEW dataset	Chemical formula	Average valence state (AVS)					
		C	S	H	Mn	Fe	O
CO2	CO_2	4		1			–2
CH4	CH_4	–4		1			
H2S	H_2S		–2	1			
SO2	SO_2		4	1			–2
H2	H_2			0			
CO	CO	2		1			–2
ACETATE	CH_3COO^-	0		1			–2
ACETIC–A	CH_3COOH	0		1			–2
Al+3	Al^{3+}			1			
AlO2–	AlO_2^-			1			–2
AlO2(SiO)	$AlO_2(SiO_2)^-$			1			–2
BENZENE	C_6H_6	–1		1			
Ca(HCO3)	$Ca(HCO_3)^+$	4		1			–2
Ca(HCOO)	$Ca(HCOO)^+$	2		1			–2
Ca(HSiO3	$CaHSiO_3^+$			1			–2
Ca(OH)+	$CaOH^+$			1			–2
Ca+2	Ca^{2+}						
CaCO3,aq	$CaCO_3$	4					–2
CaO,aq	CaO						–2
CaSO4,aq	$CaSO_4$		6				–2
CO3–2	CO_3^{2-}	4					–2
ETHANE	C_2H_6	–3		1			
ETHANOL	C_2H_5OH	–2		1			–2
ETHYLENE	C_2H_4	–2		1			
Fecho+	$Fe(CH_3COO)^+$	0		1		2	–2
Fecho0	$Fe(CH_3COO)_2$	0		1		2	–2
Fe(HSiO3	$FeHSiO_3^+$			1		2	–2
Fe(OH)+	$FeOH^+$			1		2	–2
Fe+2	Fe^{2+}					2	–2
Fe+3	Fe^{3+}					3	–2
FeO,aq	FeO					2	–2
FORMATE	$HCOO^-$	2		1			–2
FORMIC–A	$HCOOH$	2		1			–2
GLUTARAT	$C_5H_6O_4^{2-}$	0		1			–2
GLUTARIC	$C_5H_8O_4$	0		1			–2
GLYCOLAT	$C_2H_3O_3^-$	1		1			–2
GLYCOLIC	$C_2H_4O_3$	1		1			–2
H+	H^+			1			
HAlO2,aq	$HAlO_2$			1			–2
HCO3–	HCO_3^-	4		1			–2
HEXANE	C_6H_{14}	–2.33		1			
HFeO2–	$HFeO_2^-$			1		2	–2
HO2–	HO_2^-			1			–1
HS–	HS^-		–2	1			
HSiO3–	$HSiO_3^-$			1			–2
HSO3–	HSO_3^-		4	1			–2
HSO4–	HSO_4^-		6	1			–2
HSO5–	$HO–O–SO_3^-$		6	1			–1.6
Isobutan	C_4H_{10}	–2.5		1			

Fluid speciation in DEW dataset	Chemical formula	Average valence state (AVS)					
		C	S	H	Mn	Fe	O
K+	K^+						
KOH,aq	KOH			1			–2
KSO4–	KSO_4^-		6				–2
LACTATE	$C_3H_5O_3^-$	0		1			–2
LACTIC–A	$C_3H_6O_3$	0		1			–2
METHANOL	CH_3OH	–2		1			–2
Mg(HCO3)	$Mg(HCO_3)^+$	4		1			–2
Mg(HSiO3	$MgHSiO_3^+$			1			–2
Mg+2	Mg^{2+}						
MgCO3,aq	$MgCO_3$	4					–2
MgO,aq	MgO						–2
MgOH+	$MgOH^+$			1			–2
MgSO4,aq	$MgSO_4$		6				–2
Mn+2	Mn^{2+}				2		–2
MnO4–	MnO_4^-				7		–2
MnO4–2	MnO_4^{2-}				6		–2
MnSO4,aq	$MnSO_4$		6		2		–2
Na(Ac)	$NaCH_3COO$	0		1			–2
Na(Ac)2–	$Na(CH_3COO)_2^-$	0		1			–2
Na+	Na^+						
NaCO3–	$NaCO_3^-$	4					–2
NaHCO3	$NaHCO_3$	4		1			–2
NaHSiO3	$NaHSiO_3$			1			–2
NaOH,aq	$NaOH$			1			–2
OH–	OH^-			1			–2
PROPANE	C_3H_8	–2.67		1			
PROPANOA	$C_2H_5COO^-$	–0.67		1			–2
PROPANOI	C_2H_5COOH	–0.67		1			–2
PROPANOL	C_3H_7OH	–2		1			–2
S2–2	S_2^{2-}		–1				
S2O3–2	$S_2O_3^{2-}$		2				–2
S2O4–2	$S_2O_4^{2-}$		3				–2
S2O5–2	$S_2O_5^{2-}$		4				–2
S2O6–2	$S_2O_6^{2-}$		5				–2
S2O8–2	$S_2O_8^{2-}$		6				–1.75
S3–	S_3^-		–0.33				–2
S3–2	S_3^{2-}		–0.67				–2
S3O6–2	$S_3O_6^{2-}$		3.33				–2
S4–2	S_4^{2-}		–0.5				–2
S4O6–2	$S_4O_6^{2-}$		2.5				–2
S5–2	S_5^{2-}		–0.4				–2
S5O6–2	$S_5O_6^{2-}$		2				–2
Si2O4,aq	Si_2O_4						–2
Si3O6,aq	Si_3O_6						–2
SiO2,aq	SiO_2						–2
SO3–2	SO_3^{2-}		4				–2
SO4–2	SO_4^{2-}		6				–2
TOLUENE	C_7H_8	–1.14		1			

Supplementary Table 2. Solid–solution models considered in this study.

Phase	Abbreviation	Used for				Reference
Fluid	COH–Fluid	A	B	C	D	Connolly and Galvez [1]
Epidote	Ep(HP11)	A	B	C	D	Holland and Powell [2]
Chlorite	Chl(W)	A	B	C	D	White et al. [3]
Garnet	Gt(WPH)	A	B	C		White et al. [4]
Amphibole	cAmph(G)	A	B	C	D	Green et al. [5]
White mica	Mica(W)	A	B	C		White et al. [3]
Orthopyroxene	Opx(W)	A	B	C	D	White et al. [3]
Pyrrhotite	Po(HP)	A	B	C	D	Holland and Powell [2]
Pumpellyite	Pu	A	B	C	D	Massonne and Willner [6]
Chloritoid	Ctd(W)	A	B	C	D	White et al. [3]
Dolomite	Do(HP)	A	B	C	D	Holland and Powell [7]
Magnesite	M(HP)	A	B	C	D	Holland and Powell [7]
Brucite	B	A	B	C	D	Holland and Powell [7]
Talc	T		B	C	D	Holland and Powell [7]
Dolomite	Do(HP)	A	B	C	D	Holland and Powell [7]
Magnesite	M(HP)	A	B	C	D	Holland and Powell [7]
Biotite	Bi(W)	A	B	C		White et al. [3]
Antigorite	Atg(LE)	A	B	C	D	Eberhard et al. [8]
Lizardite	Liz(LE)	A	B	C	D	Eberhard et al. [8]
Spinel	Sp(JH)	A	B	C	D	Jennings and Holland [9]
Clinopyroxene	Omph(GHP)	A	B	C		Green et al. [10] revised in 2016
Olivine	O(JH)	A	B	C	D	Jennings and Holland [9]
Clinopyroxene	Cpx(JH)				D	Jennings and Holland [9]
Garnet	Grt(JH)				D	Jennings and Holland [9]
Feldspar	lAb(HGP)	A	B	C		Holland et al. [11] updated in 2024
	Fsp(HGP)	A	B	C		Holland et al. [11]
Melt	Melt(G25)	A	B	C	D	Holland et al. [12] and Green et al. [13]

Solution models used for thermodynamic modeling: A, the studied eclogite and pristine oceanic basalt; B, average gabbro; C, deep-seated gabbro; D, serpentinite.

The DQF of f3clin used for modeling serpentinite was set to 40000 J/mol Eberhard et al. [8].

Supplementary Texts

Supplementary Text 1. Study area and geological context

The South Tianshan orogenic belt, extending over 2000 km in Central Asia, is defined by several discrete HP–UHP belts. These belts stretch from the Fan–Karategin belt in Tajikistan in the west, through the Atbashi belt in Kyrgyzstan, to the Southwestern Tianshan belt in China in the east [14]. The Southwestern Tianshan HP–UHP metamorphic belt in China is a well–exposed, wedge–shaped unit situated between the Yili–Central Tianshan and Tarim plates. This belt represents remnants of the Paleo–South Tianshan oceanic lithosphere that was subducted northward beneath the Yili–Central Tianshan plate during the late Paleozoic [14]. It comprises metabasites, metasedimentary rocks, marble, and serpentinized ultramafic bodies accompanied by rodingite. In the Akeyazi area, eclogite, blueschist and amphibolite occur as interlayers or lenticular blocks in the metasediments and record peak eclogite–facies conditions of 2.8–3.2 GPa at 430–580 °C, reflecting a clockwise P–T evolution and consistent with the presence of coesite [15–18]. Serpentinites, together with associated rodingites, metabasites (e.g., eclogite, blueschist, and greenschist), and ophicarbonates, constitute ultramafic complexes that are commonly interpreted as hydrated ophiolitic mantle [19,20]. These lenses are enclosed within metapelites near the Changawuzi Fault in the Muzhaerte area [19,21,22] and contain Ti–chondrodite-bearing ultramafic rocks that record peak pressures of 3.7 ± 0.7 GPa at 510–530 °C and 4.1–4.3 GPa at ~460 °C [21,23]. Lawsonite-bearing eclogites reported in the same area yield 2.8–3.2 GPa at 480–590 °C [24]. These results reveal a cold regime in the SW Tianshan subduction, with a geothermal gradient of 5–6 °C/km. Field observations also document abundant HP veins in the belt, characterized by assemblages rich in omphacite, garnet, epidote, rutile, carbonate, or quartz. This indicates episodic fluid pulses and intense fluid–rock interaction within the slab interior during deep subduction, with fluids sourced both internally and externally [25–27].

Supplementary Text 2. Hypothesis of CH_4–H_2 formation in the oceanic crust

The evolution of COH fluids in subduction zones is governed by the P–T–fO_2 conditions of the fluid–rock system [28], which are controlled by two mechanisms: (1) internal devolatilization, where fluid composition is regulated by equilibrium with the host rock under low fluid–rock ratios (i.e., rock–buffered systems), and (2) external fluid infiltration and metasomatism, controlled by the properties and fluxes of incoming fluids, including their redox state and dissolved species (i.e., fluid–buffered systems). The redox budget (RB) is controlled by the protolith composition and is likely modified by devolatilization and fluid–rock interactions along the subduction P–T path. Lower RB in the system typically promotes the formation of more reduced fluids (e.g., CH_4–H_2-rich fluids). Bulk–rock compositions of the CH_4±H_2-bearing eclogites in the SW Tianshan exhibit substantial chemical heterogeneity, with CO_2 contents of 0.62–10.48 wt.% and $Fe^{3+}/\Sigma Fe$ ratios of 0.198–0.392, both markedly higher than those of pristine oceanic basalt and comparable to AOC (Extended Data Table 1). On this basis, we calculated the speciation of carbon– and sulfur-bearing phases, the AVS of carbon and the RB in fluids equilibrated with the rock, as well as the system fO_2 (Supplementary Fig. 1), starting from a RB reference of the eclogite (H19–43–2) and progressively adding O_2 to the system under fluid–saturated conditions (~7 wt.% H_2O). For the fluid–rock system, CH_4–dominated reduced fluids are expected to be stable in the pyrrhotite–graphite stability field at ΔFMQ < –2. This is markedly lower than those required to stabilize the dolomite + graphite + omphacite + quartz assemblage in the matrix, which records buffering by the reaction $CaMgSi_2O_6$ (in omphacite) + C + O_2 = $CaMg(CO_3)_2$ + SiO_2) at conditions approaching FMQ ~0, and is consistent with modeling resultes constrained by the measured bulk–rock composition [29] (Supplementary Fig. 1). Petrological observations show that CH_4−FIs−bearing garnet contains disseminated graphite but no carbonate minerals, whereas pyrite, carbonate minerals such as dolomite occur predominantly in the matrix. The modeled fluids equilibrated with the carbonate-bearing assemblage are CO_2–dominated (AVS_C > +3) and relatively oxidizing (ΔFMQ > 0). Therefore, altered oceanic crust (AOC) with high carbonate content (> 0.7 wt.%) and high $Fe^{3+}/\Sigma Fe$ ratios (0.20 to >0.60) [30,31], equilibrium devolatilization during subduction is unlikely to generate such reduced, CH_4–H_2-rich fluids. Our results support the prevailing view that AOC-derived fluids are relatively oxidizing [32]. Given that the measured bulk composition is enriched in ferric iron and contains Fe-bearing dolomite, it is difficult to confidently assess the extent of protolith modification in the Tianshan eclogites. In other words, the oxygen fugacity recorded during garnet core growth and CH_4 formation in these rocks was significantly lower than that predicted by models based on the measured bulk composition. This redox discrepancy suggests either oxidation–driven modification of the bulk composition during metamorphism or infiltration of an externally derived reduced fluid during garnet growth.

Supplementary Text 3. Influence of initial hydration degree on fO_2 in fluid–rock systems

Water exerts a profound influence on both the mineral assemblage and redox state of equilibrated rocks. A well–known example is the deep dserpentinization of ultramafic rocks, during which magnetite and H_2 are produced, driving the fluid–rock system toward markedly lower fO_2. Beyond ultramafic systems, basaltic oceanic crust, with varying degree of hydration, defined as the ratio of the initial added H_2O content to the initial H_2O content at saturation, may also exhibit a range of redox states under different P–T conditions in subduction zones. The initial H_2O content at saturation was taken as the maximum H_2O content at 200 °C (~5.25 wt.%), as calculated using Perple_X. We performed thermodynamic devolatilization modeling, using a representative CH_4–H_2-bearing eclogite composition (H19-43-2), to assess the effects of initial rock hydration degrees (Extended Data Fig. 1). Details of the initial bulk–rock composition and the modeling approaches used to define the slab P–T path, phase equilibria, and fluid speciation are provided in the Supplementary Table 2 (Extended Data Fig. 2 and Supplementary Fig. 2). The modeling results show that, overall, increasing degrees of rock hydration lead to a progressive decrease in system fO_2 at temperatures below ~540 °C, from ΔFMQ of +3.6 to +0.7 at 200 °C to ΔFMQ of +2.3 to –0.2 at 540 °C. Initial hydration degree from 0 to ~20% produces little change in fO_2, whereas hydration exceeding ~20% leads to a marked decrease, which plateaus after ~60%. Beyond ~60 % initial hydration, however, the system fO_2 remains essentially constant or shows only a very minor increase (<0.3 log units relative to FMQ). To further elucidate the influence of water, we determined the mineral assemblages and the contributions of different minerals to the redox budget (RB), which quantifies a system's redox capacity along the subduction trajectory for initial hydration degrees of 20 %, 40 %, 60 %, 80 % and 100 %. In the carbonate-bearing eclogite, the bulk–rock RB is dominated by clinopyroxene, glaucophane, and carbonates (>95%), whereas garnet, pyrite, anhydrite, and white mica constitute less than 5% (Extended Data Fig. 1). Increasing water content has a negligible influence on the bulk–rock RB, which decreases only slightly from 0.2630 at 20% hydration to 0.2521 at 100%. Following the mineral abbreviations of ref. [33], the following mineral end-member compositions are as: the clinopyroxene end-member: Jd–jadeite ($NaAlSi_2O_6$), Hed–hedenbergite ($CaFeSi_2O_6$), Aeg–aegirine ($NaFe^{3+}Si_2O_6$); the garnet end-member: Andr–andradite ($Ca_3Fe^{3+}{}_2Si_3O_{12}$), Prp–pyrope ($Mg_3Al_2Si_3O_{12}$); the Fe^{3+}-bearing sodic amphibole endmember: Mrbk–magnesioriebeckite [$Na_2Mg_3Fe^{3+}{}_2Si_8O_{22}(OH)_2$], Lws–lawsonite [$CaAl_2Si_2O_7(OH)_2·H_2O$], Sid–siderite ($FeCO_3$), Qz–quartz ($SiO_2$), and Gr–graphite (C).

At initial hydration degrees less than 60 %, the primary effect of water addition facilitates the formation of hydrous minerals, such as lawsonite and minor glaucophane (Supplementary Fig. 3), while carbon remains stored in carbonate minerals. The redox buffering may be schematically expressed as:

$$7Andr + 2Jd + 15Qz + 6H_2O + 2Alm = 2Aeg + 3Lws + 18Hed + 3O_2$$

This process is coupled with hydration reactions that stabilize hydrous minerals, depending on bulk–rock composition. Increasing water content also favors the incorporation of ferric iron into clinopyroxene, as indicated by the modeling results (Supplementary Fig. 4). Although the redox budget shows little overall variation, enhanced partitioning of Fe^{3+} into clinopyroxene drives a decrease in system fO_2. The Fe^{3+} content of clinopyroxene has been shown to correlate with H_2O content and can exceed 30% of total iron (Fe_{total}), with Fe^{3+}/Fe_{total} reaching >50% [34,35].

At initial hydration degrees greater than 60%, hydrous minerals continue to increase, while carbonate is progressively reduced to graphite. This redox buffering may be schematically written as:

$$12Sid + 38Jd + 28Hed + 3Qz + 6Prp + 56H_2O = 26Aeg + 1Andr + 25Lws + 6Mrbk + 2O_2 + 12Gr$$

In this regime, coexistence of newly formed graphite with residual carbonate efficiently buffers fO_2, so electron transfer between silicates and carbonates has little effect on the redox state. At low temperature, garnet, pyrite, and white mica remain subordinate and contribute only minimally to the rock redox budget, whereas clinopyroxene and sodic amphibole dominate the redox budget because of their strong capacity to host Fe^{3+}. Together, these results show that increasing hydration promotes lawsonite formation, drives Fe^{3+} enrichment in clinopyroxene and amphibole, and facilitates carbonate reduction to graphite.

References

1. Connolly, J. A. D. & Galvez, M. E. Electrolytic fluid speciation by Gibbs energy minimization and implications for subduction zone mass transfer. *Earth and Planetary Science Letters* **501**, 90–102 (2018).
2. Holland, T. J. B. & Powell, R. An improved and extended internally consistent thermodynamic dataset for phases of petrological interest, involving a new equation of state for solids. *Journal of Metamorphic Geology* **29**, 333–383 (2011).
3. White, R. W., Powell, R., Holland, T. J. B., Johnson, T. E. & Green, E. C. R. New mineral activity–composition relations for thermodynamic calculations in metapelitic systems. *Journal Metamorphic Geology* **32**, 261–286 (2014).
4. White, R. W., Powell, R. & Holland, T. J. B. Progress relating to calculation of partial melting equilibria for metapelites. *Journal Metamorphic Geology* **25**, 511–527 (2007).
5. Green, E. C. R. *et al.* Activity–composition relations for the calculation of partial melting equilibria in metabasic rocks. *Journal Metamorphic Geology* **34**, 845–869 (2016).
6. Massonne, H. J. & Willner, A. P. Phase relations and dehydration behaviour of psammopelite and mid-ocean ridge basalt at very-low-grade to low-grade metamorphic conditions. *ejm* **20**, 867–879 (2008).
7. Holland, T. J. B. & Powell, R. An internally consistent thermodynamic data set for phases of petrological interest. *Journal Metamorphic Geology* **16**, 309–343 (1998).
8. Eberhard, L., Frost, D. J., McCammon, C. A., Dolejš, D. & Connolly, J. A. D. Experimental Constraints on the Ferric Fe Content and Oxygen Fugacity in Subducted Serpentinites. *Journal of Petrology* **64**, egad069 (2023).
9. Jennings, E. S. & Holland, T. J. B. A Simple Thermodynamic Model for Melting of Peridotite in the System NCFMASOCr. *Journal of Petrology* **56**, 869–892 (2015).
10. Green, E., Holland, T. & Powell, R. An order-disorder model for omphacitic pyroxenes in the system jadeite-diopside-hedenbergite-acmite, with applications to eclogitic rocks. *American Mineralogist* **92**, 1181–1189 (2007).
11. Holland, T. J. B., Green, E. C. R. & Powell, R. A thermodynamic model for feldspars in $KAlSi_3O_8$-$NaAlSi_3O_8$-$CaAl_2Si_2O_8$ for mineral equilibrium calculations. *Journal Metamorphic Geology* **40**, 587–600 (2022).
12. Holland, T. J. B., Green, E. C. R. & Powell, R. Melting of Peridotites through to Granites: A Simple Thermodynamic Model in the System KNCFMASHTOCr. *Journal of Petrology* **59**, 881–900 (2018).
13. Green, E. C. R., Holland, T. J. B., Powell, R., Weller, O. M. & Riel, N. Corrigendum to: Melting of Peridotites through to Granites: a Simple Thermodynamic Model in the System KNCFMASHTOCr, and, a Thermodynamic Model for the Subsolidus Evolution and Melting of Peridotite. *Journal of Petrology* **66**, egae079 (2025).
14. Zhang, L., Wang, Y., Zhang, L. & Lü, Z. Ultrahigh pressure metamorphism and tectonic evolution of southwestern Tianshan orogenic belt, China: a comprehensive review. *SP* **474**, 133–152 (2019).
15. Tao, R. *et al.* Formation of abiotic hydrocarbon from reduction of carbonate in subduction zones: Constraints from petrological observation and experimental simulation. *Geochimica et Cosmochimica Acta* **239**, 390–408 (2018).
16. Lü, Z., Zhang, L., Du, J. & Bucher, K. Petrology of coesite-bearing eclogite from Habutengsu Valley, western Tianshan, NW China and its tectonometamorphic implication. *Journal Metamorphic Geology* **27**, 773–787 (2009).
17. Tian, Z. L. & Wei, C. J. Metamorphism of ultrahigh-pressure eclogites from the Kebuerte Valley, South Tianshan, NW China: phase equilibria and *P–T* path. *Journal Metamorphic Geology* **31**, 281–300 (2013).
18. Tan, Z. *et al.* P–T–time-isotopic evolution of coesite-bearing eclogites: Implications for exhumation processes in SW Tianshan. *Lithos* **278–281**, 1–25 (2017).
19. Li, X., Zhang, L., Wei, C., Ai, Y. & Chen, J. Petrology of rodingite derived from eclogite in western Tianshan, China. *Journal Metamorphic Geology* **25**, 363–382 (2007).
20. Shen, T. *et al.* In-situ U–Pb dating and Nd isotopic analysis of perovskite from a rodingite blackwall associated with UHP serpentinite from southwestern Tianshan, China. *Chemical Geology* **431**, 67–82 (2016).
21. Shen, T. *et al.* UHP Metamorphism Documented in Ti-chondrodite- and Ti-clinohumite-bearing Serpentinized Ultramafic Rocks from Chinese Southwestern Tianshan. *J. Petrology* **56**, 1425–1458 (2015).
22. Peng, W. *et al.* Multistage CO2 sequestration in the subduction zone: Insights from exhumed carbonated serpentinites, SW Tianshan UHP belt, China. *Geochimica et Cosmochimica Acta* **270**, 218–243 (2020).
23. Tang, Y. & Shen, T. Petrological characteristics and metamorphic evolution of serpentinized harzburgite

from Chinese southwestern Tianshan. *Acta Petrologica Sinica* **41**, 3782–3801 (2025).

24. Lü, Z., Zhang, L., Yue, J. & Li, X. Ultrahigh-pressure and high- *P* lawsonite eclogites in Muzhaerte, Chinese western Tianshan. *Journal Metamorphic Geology* **37**, 717–743 (2019).
25. John, T., Klemd, R., Gao, J. & Garbe-Schönberg, C.-D. Trace-element mobilization in slabs due to non steady-state fluid–rock interaction: Constraints from an eclogite-facies transport vein in blueschist (Tianshan, China). *Lithos* **103**, 1–24 (2008).
26. Beinlich, A., Klemd, R., John, T. & Gao, J. Trace-element mobilization during Ca-metasomatism along a major fluid conduit: Eclogitization of blueschist as a consequence of fluid–rock interaction. *Geochimica et Cosmochimica Acta* **74**, 1892–1922 (2010).
27. Gong, T.-N. *et al.* Mineral precipitation sequence from multi-stage fluids released by eclogite during high-pressure metamorphism. *American Mineralogist* **110**, 136–153 (2025).
28. Ague, J. J. *et al.* Slab-derived devolatilization fluids oxidized by subducted metasedimentary rocks. *Nat. Geosci.* **15**, 320–326 (2022).
29. Wang, C., Tao, R., Walters, J. B., Höfer, H. E. & Zhang, L. Favorable P–T–fO_2 conditions for abiotic CH_4 production in subducted oceanic crusts: A comparison between CH_4-bearing ultrahigh- and CO_2-bearing high-pressure eclogite. *Geochimica et Cosmochimica Acta* **336**, 269–290 (2022).
30. Bach, W. & Edwards, K. J. Iron and sulfide oxidation within the basaltic ocean crust: implications for chemolithoautotrophic microbial biomass production. *Geochimica et Cosmochimica Acta* **67**, 3871–3887 (2003).
31. Stolper, D. A. & Keller, C. B. A record of deep-ocean dissolved O_2 from the oxidation state of iron in submarine basalts. *Nature* **553**, 323–327 (2018).
32. Walters, J. B., Cruz-Uribe, A. M. & Marschall, H. R. Sulfur loss from subducted altered oceanic crust and implications for mantle oxidation. *Geochem. Persp. Let.* 36–41 (2020).
33. Whitney, D. L. & Evans, B. W. Abbreviations for names of rock-forming minerals. *American Mineralogist* **95**, 185–187 (2010).
34. Maffeis, A. *et al.* Filling the gap in the UHP metamorphic record of the Liguro-Piemont Lower unit: Insights on fluid-mediated formation of atoll garnets. *Lithos* **498–499**, 107981 (2025).
35. Marras, G., Mikhailenko, D., McCammon, C. A., Agasheva, E. & Stagno, V. Ferric Iron in Eclogitic Garnet and Clinopyroxene from the V. Grib Kimberlite Pipe (NW Russia): Evidence of a Highly Oxidized Subducted Slab. *Journal of Petrology* **65**, egae054 (2024).